

# Phase Frustration-Induced Spatial Lattice Symmetry in the Vicsek-Kuramoto-Sakaguchi Model

Yichen Lu

November 3, 2025

## Contents

<b>1</b>	<b>The Model</b>	<b>1</b>
<b>2</b>	<b>Lattice Structures and Spatiotemporal Patterns</b>	<b>3</b>
<b>3</b>	<b>Respiration-like motion of unit cells [In future publications]</b>	<b>5</b>
<b>4</b>	<b>Dominant-Recessive Lattice and Hyperuniformity</b>	<b>7</b>
<b>5</b>	<b>Initial conditions determined cells composition [In future publications]</b>	<b>9</b>
<b>6</b>	<b>Critical transition and mechanism</b>	<b>10</b>
<b>7</b>	<b>Conclusions</b>	<b>12</b>

## 1 The Model

Particles are characterized by their spatial position  $\mathbf{r}_i = (x_i, y_i)$  and a phase angle  $\theta_i$ , whose dynamics are governed by the following equations:

$$\dot{\mathbf{r}}_i = v\mathbf{p}(\theta_i) , \quad (1a)$$

$$\dot{\theta}_i = \frac{K}{|A_i|} \sum_{j \in A_i} [\sin(\theta_j - \theta_i + \alpha) - \sin \alpha] , \quad (1b)$$

for  $i = 1, 2, \dots, N$ . Here in Eq. (1a),  $\mathbf{p}(\theta) = (\cos \theta, \sin \theta)$  denotes the direction vector, implying that each particle moves at a constant speed  $v$  along the direction of its instantaneous phase  $\theta_i(t)$ . According to Eq. (1b), the phase evolution involves a local average over neighbors within a coupling radius  $d_0$  of particle  $i$ :

$$A_i(t) = \{j \mid |\mathbf{r}_i(t) - \mathbf{r}_j(t)| \leq d_0\} , \quad (2)$$

where  $K (\geq 0)$  represents the coupling strength and  $\alpha$  is the phase frustration between two neighboring particles. The introduction of counter term  $-\sin \alpha$  ensures that the frustration vanishes exactly when phase differences vanish ( $\theta_j - \theta_i = 0$ ), thereby guaranteeing that perfect synchronization remains an equilibrium state. Without this term, synchronized oscillators would experience a net force  $K \sin \alpha$ , artificially shifting their frequencies [9]. This model generalizes both aligning [4, 7, 8, 12, 13] and anti-aligning [2, 3] interaction models. When  $\alpha_0 = 0$ , the dynamics reduces to the Vicsek-Kuramoto model. In the case where  $\alpha = \pi$ , the system exhibits anti-aligning interactions, causing particles to adopt phases opposite to those of their neighbors.

Some necessary order parameters can be introduced to measure the level of coordination among particles in space motion and phase dynamics. Firstly, at the macroscopic level, the system may be

described by the single-partial distribution  $\rho(\mathbf{r}, \theta, t)$ , which satisfies the normalization condition

$$\int_{L \times L} d^2\mathbf{r} \int_0^{2\pi} d\theta \rho(\mathbf{r}, \theta, t) = 1, \quad (3)$$

where  $L$  is the size of the system in two dimensions. Next, we define the coarse-grained spatial density  $\varrho(\mathbf{r}, t)$  and the global polarization  $p(\theta, t)$  density by integrating  $\rho(\mathbf{r}, \theta, t)$  over the phase and spatial, respectively:

$$\varrho(\mathbf{r}, t) = \int_0^{2\pi} \rho(\mathbf{r}, \theta, t) d\theta, \quad (4a)$$

$$p(\theta, t) = \int_{L \times L} \rho(\mathbf{r}, \theta, t) d\mathbf{r}. \quad (4b)$$

In the homogeneous state, these quantities take uniform values  $(\rho, \varrho, p) = (\rho_0, \varrho_0, p_0) = (1/(2\pi L^2), 1/L^2, 1/2\pi)$ .

To measure deviations from uniformity, we define the following single-particle order parameters:

$$\rho_{\text{std}}(t) = \frac{1}{1 - \rho_0} \left[ \max_{\mathbf{r} \in L \times L, \theta \in [0, 2\pi]} \rho(\mathbf{r}, \theta, t) - \rho_0 \right], \quad (5)$$

Similarly, we can define order parameters for spatial and phase polarization densities, denoted as  $\varrho_{\text{std}}$  and  $p_{\text{std}}$ , respectively. These order parameters range from 0 to 1, reflecting the degree of spatial and phase coherence in the system. When particles are uniformly distributed in both space and phase,  $\rho, \varrho, p_{\text{std}} \approx 0$ . Conversely, if full condensation and polarization occur,  $\rho, \varrho, p_{\text{std}} \approx 1$ .

We conducted numerical simulations to investigate the performance and characteristics of our system under various conditions. For simplicity, we assume that particles are initially distributed uniformly in a two-dimensional  $L \times L$  square with periodic boundary conditions. Unless otherwise stated, all the numerical simulations of the model Eq. (1) were run on Python using Euler integration. For the final state and phase diagram, each data point of order parameters was collected by averaging last 500 time steps of the simulation to discard the transients.

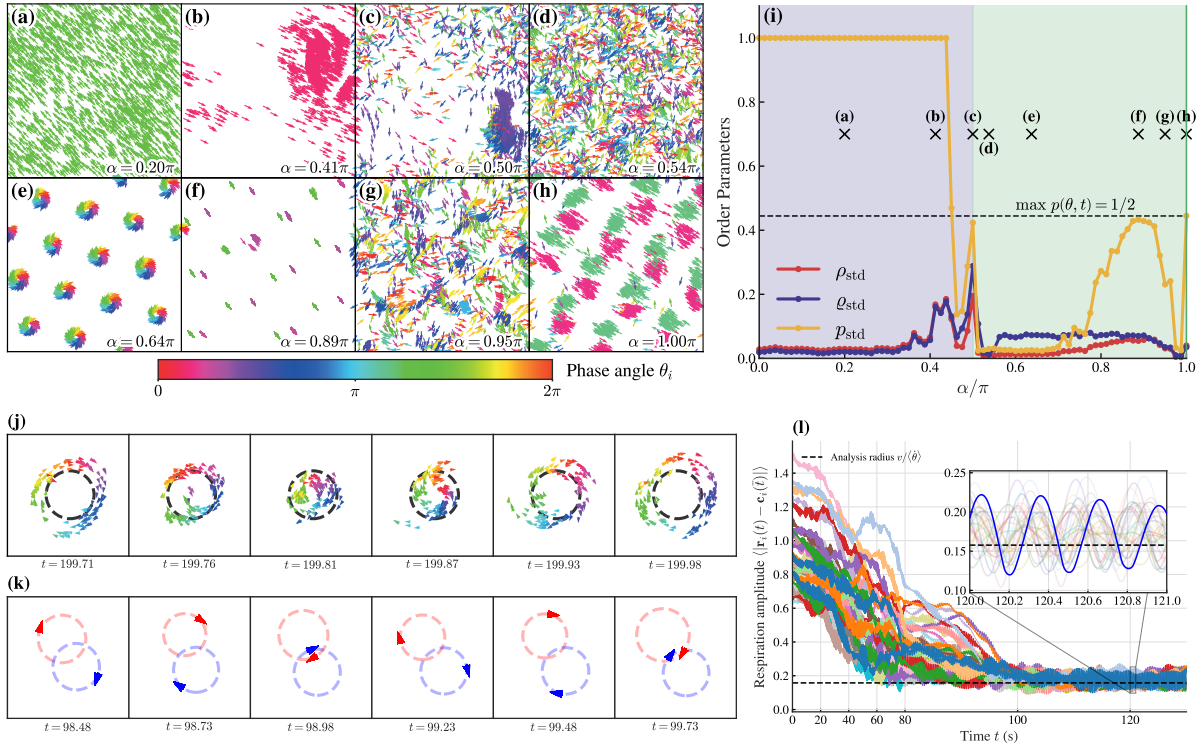


Figure 1: (a)-(h) Representative simulation snapshots for synchronization state [(a)-(c)] and lattice state [(d)-(h)] at different phase frustration  $\alpha$ . The orientation and color of particles represent their instantaneous phase  $\theta_i$ . (i) Phase diagram and order parameters of the system with respect to the phase frustration  $\alpha$ . The crosses mark the snapshots in (a)-(h). Regions of blue and green respectively represent the synchronization and lattice states. The horizontal dashed line indicates the values of the value of order parameter  $p_{\text{std}}$  when  $\max p(\theta, t) = 1/2$  (Dual cluster synchronization). (j), (k) Time evolution of respiration motion of vortex [(j),  $\alpha = 0.6\pi$ ] and double clustered [(k),  $\alpha = 0.9\pi$ ] unit cell. (k) The red and blue arrows represent the two clusters divided by their phases, and dashed circles of corresponding colors are estimated motion trajectories based on their instantaneous effective frequencies in Eq. (6). (l) Respiration amplitude revealed by the time evolution for  $\alpha = 0.6\pi$ . Other parameters:  $K = 20$ ,  $d_0 = 1.55$ ,  $L = 7$ ,  $N = 2000$ ,  $v = 3$ .

## 2 Lattice Structures and Spatiotemporal Patterns

Our system consists of self-propelled particles with local phase interactions, leading to a rich variety of collective behaviors. As shown in Fig. 1(a), when the phase frustration  $\alpha$  is small, the system tends to synchronize in phase, resulting in a globally synchronized state where all particles move coherently in the same direction. This state is characterized by high values of the order parameter  $p_{\text{std}}$  and low values of  $\rho_{\text{std}}$  and  $\varrho_{\text{std}}$ , indicating uniform spatial distribution but strong phase coherence. As  $\alpha$  gradually increases but still maintains continuity ( $\alpha < \pi/2$ ), the system exhibits a swarming synchronization state, as shown in Fig. 1(b). In this state, particles form a large, coherent cluster that moves collectively, with phases still largely aligned. The order parameters reflect this state, with  $p_{\text{std}}$  remaining high, while  $\rho_{\text{std}}$  and  $\varrho_{\text{std}}$  bifurcate from zero due to the formation of the cluster. The parameter space and phenomena mentioned above have been extensively studied in previous works [5, 6]. With increasing  $\alpha$  beyond  $\pi/2$ , the system undergoes a transition to a lattice state, as shown in Fig. 1(d)-(h). In this state, particles arrange themselves into a hexagonal lattice structure, breaking the spatial uniformity. The order parameters reflect this change, with  $\rho_{\text{std}}$  and  $\varrho_{\text{std}}$  non-zero significantly remaining constant over a large range ( $0.55\pi < \alpha < 0.9\pi$ ), indicating the formation of spatial patterns.  $p_{\text{std}}$  decreases at first ( $0.5\pi < \alpha < 0.7\pi$ , the vortex lattice state, Fig. 1(e)), showing reduced phase coherence, but then increases again ( $0.7\pi < \alpha < \pi$ ), indicating the emergence of dual-cluster synchronization where particles

form two distinct phase clusters (Fig. 1(f)). This dual-cluster state is characterized by two clustered phases that differ by  $\pi$ , leading to a bimodal distribution in  $p(\theta, t)$ . Continuing to increase  $\alpha$  towards  $\pi$ , the three order parameters decrease again, indicating a return to a more disordered state (Fig. 1(g)). While at  $\alpha = \pi$ , system reaches a state of perfect anti-synchronization, where neighboring particles have phases differing by  $\pi$ , leading to a dual-lane pattern in space and dual-cluster synchronization in phase (Fig. 1(h)). Different from the previous dual-cluster state in Fig. 1(f), here the two phase clusters are fixed, resulting in a continuous linear arrangement of motion in space. This pattern has also been observed in Escaff's work on anti-aligning interactions [2, 3]

For a more detailed understanding of the spatiotemporal pattern for lattice states, we examined the time evolution of individual unit cells in the vortex lattice and dual-cluster states, as shown in Fig. 1(j) and (k). In the vortex lattice state (Fig. 1(j)), particles within a unit cell exhibit a respiration motion, where they periodically expand and contract around their analysis average radius  $v/\langle\dot{\theta}\rangle$ , where  $\langle\dot{\theta}\rangle$  is given by the phase dynamics in incoherent states

$$\begin{aligned}\langle\dot{\theta}\rangle &= -K \sin \alpha + \frac{K}{2\pi} \int_0^{2\pi} d\theta' \sin(\theta' - \theta + \alpha) \\ &= -K \sin \alpha.\end{aligned}\tag{6}$$

This dynamic behavior is characterized by oscillations in the distance between particles and the centers of their unit cells  $|\mathbf{r}_i(t) - \mathbf{c}_i(\bar{t})|$ , as illustrated in Fig. 1(l), where  $\mathbf{c}_i(\bar{t})$  is the center of the unit cell averaged over one period. The amplitude of these oscillations provides insight into the stability of the lattice structure (see Hopf–Turing bifurcation in Sec. 6). As respiration motion, compared to the vortex lattice state, the dual-cluster state (Fig. 1(k)) shows a more ordered arrangement, with two groups of particles rotating around the center of the unit cell in opposite directions along approximately fixed trajectory (Note that they are not only two particles but two groups of particles fully condensed). The trajectories of these two groups can be approximated by circles with radii determined by their instantaneous effective frequencies in Eq. 6, as indicated by the dashed circles in Fig. 1(k).

### 3 Respiration-like motion of unit cells [In future publications]

For  $\alpha = 0.6\pi$ , the system exhibits the respiration-like motion of the cells. Since the phases of particles in each cell are uniformly distributed in  $[0, 2\pi]$  and the distance between cells is large enough to be considered decoupled, the effective frequency of each particle can be approximated by

$$\dot{\theta}_i = -K \sin \alpha + \frac{K}{|A_i|} \int_0^{2\pi} d\theta' \sin(\theta' - \theta_i + \alpha) = -K \sin \alpha , \quad (7)$$

and the lattice constant  $a$  can be approximated as

$$a = d_0 + 2 \frac{v}{K |\sin \alpha|} . \quad (8)$$

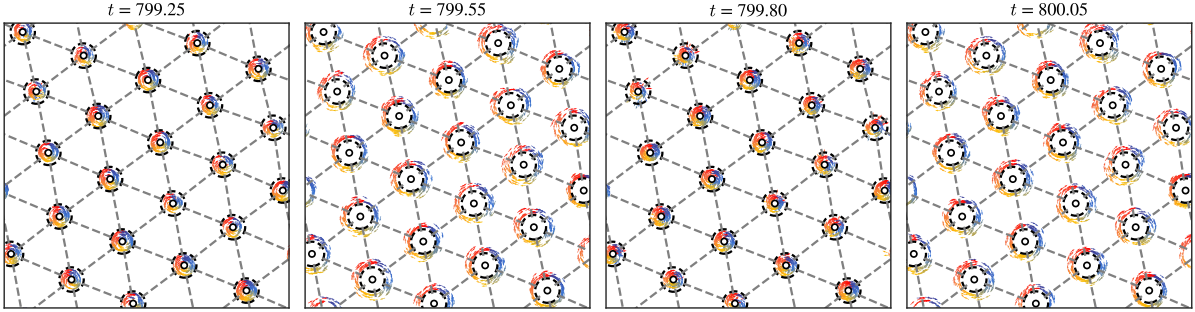


Figure 2: respiration-like motion of the cells with  $\omega_{\min} = 0$ ,  $\Delta\omega = 1$ ,  $N = 3000$ ,  $K = 10.5$ ,  $d_0 = 1.07$ , and  $\alpha = 0.6\pi$ . Black hollow dots represent the center of mass of each cell, black dash circles represent the theoretical unit cell radius  $v/\dot{\theta}_i$ , and the gray dash lines represent the theoretical distance between unit cells  $d_0$ .

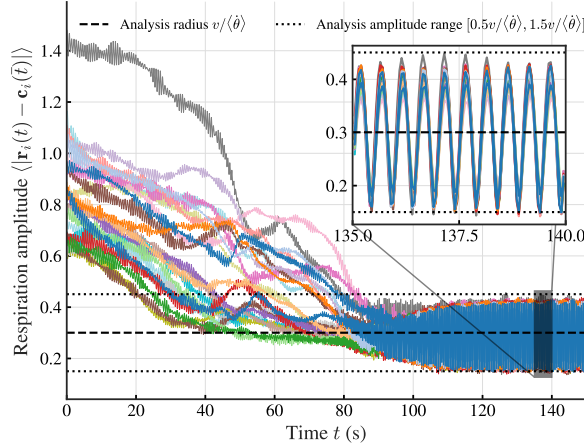


Figure 3: respiration amplitude of the system. The parameters are the same as in Fig. 2. Different colors represent different cells, and the amplitude is defined as the distance between particles and the center of mass of the cell at final state ( $\bar{t} = 40$ ).

As shown in Fig. 2 and Fig. 3, the respiration amplitude of the cells is defined as  $\langle |\mathbf{r}_i(t) - \mathbf{c}_i(\bar{t})| \rangle$ , where  $\mathbf{c}_i(\bar{t})$  is the center of mass of the cell of  $i$ -th particle at final state ( $\bar{t} = 40$ ), and  $\langle \cdot \rangle$  denotes the average over all particles in the cell. It is worth noting that the amplitude is fluctuating around the theoretical cell radius  $v/\dot{\theta}_i$  and the respiration frequency of the cells exhibit synchronization.

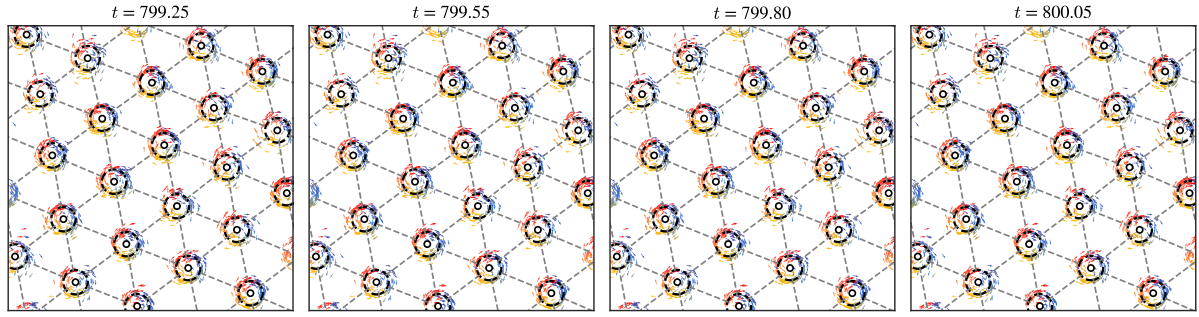


Figure 4: respiration-like motion of the decoupled cells. The parameters are the same as in Fig. 2.

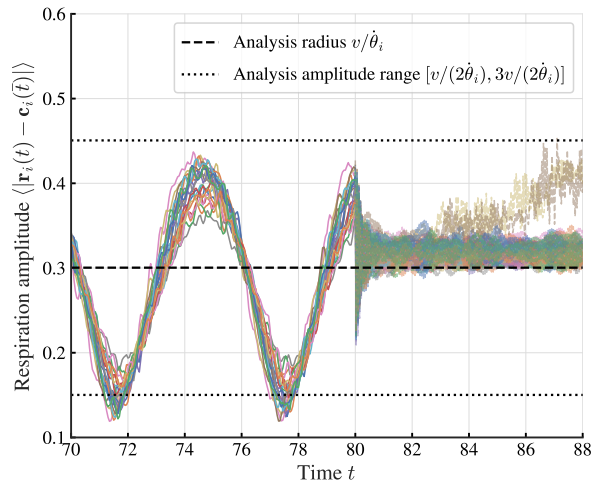


Figure 5: Respiration amplitude of the decoupled cells ( $t > 80$ ). The parameters are the same as in Fig. 2.

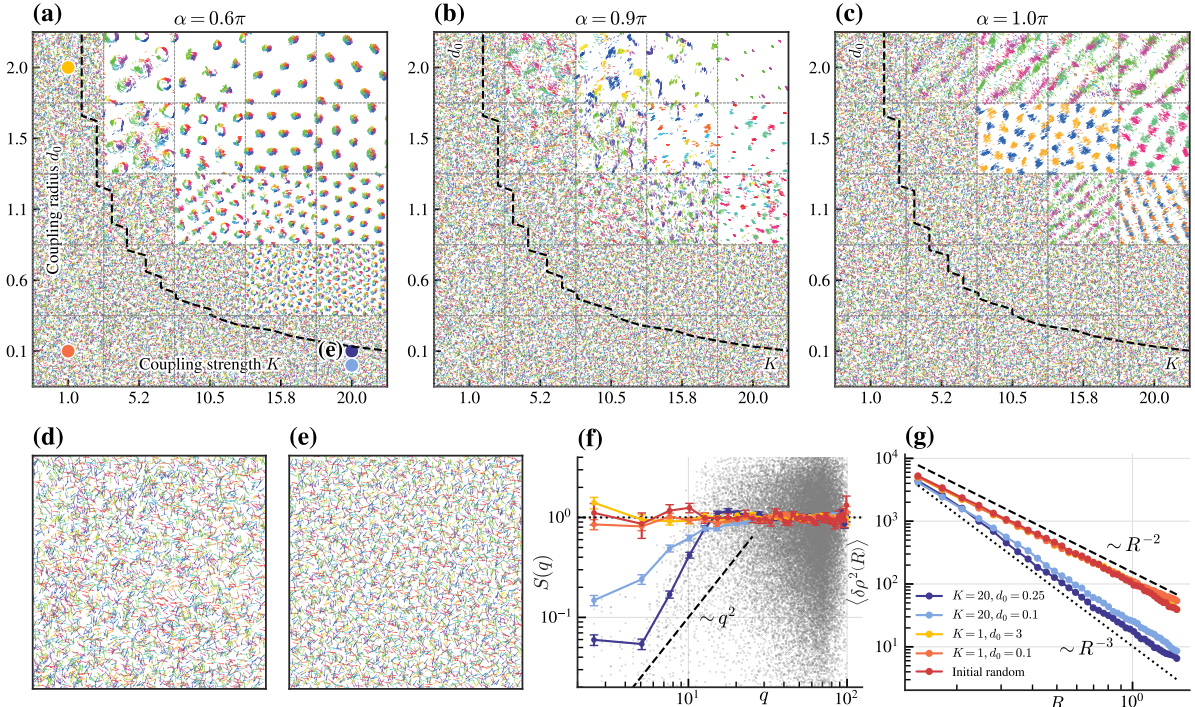


Figure 6: (a)-(c) Snapshots of  $(K, d_0)$  phase diagram under different frustration  $\alpha$  for  $L = 7, N = 2000$  and  $v = 3$ . The boundaries between dominant and recessive lattice states, determined by Eq. (20), are indicated with black dashed lines. (d), (e) Snapshots comparing random uniform initial conditions (d) and the resulting hyperuniform final state (e) for  $K = 20, d_0 = 0.25, \alpha = 0.6\pi$  and  $N = 5000$  (large population for better showcase). Hyperuniformity of the recessive lattice states is characterized by the structure factor  $S(q)$  in (f) and the density variance  $\langle \delta \rho^2(R) \rangle$  in (g). Black dashed lines indicate the scaling behaviors  $S(q) \sim q^{-2}$  and  $\langle \delta \rho^2(R) \rangle \sim R^{-2,-3}$ , respectively. In (f), gray dots represent the sample of  $S(\mathbf{q}_n)$  for periodic boundary conditions allowed wavevectors  $\mathbf{q}_n = (2\pi n_1/L, 2\pi n_2/L)$  with  $n \in (\mathbb{Z}^*)^2$  at  $K = 20, d_0 = 0.25$ , and the point-fold curves with error bars show the binned average and standard deviation of their respective  $S(\mathbf{q}_n)$ . Solid dots and text label in (a) mark the location in  $(K, d_0)$  phase diagram corresponding to the parameters analyzed in (e)-(g).

## 4 Dominant-Recessive Lattice and Hyperuniformity

As discussed above, the lattice state emerges when the phase frustration  $\alpha$  exceeds the critical value  $\pi/2$ , with  $\alpha$  primarily governing the topology of the lattice pattern. However, the prominence of this lattice structure depends on the coupling strength  $K$  and coupling radius  $d_0$ . As illustrated in Fig. 6(a)-(c), for a fixed  $\alpha$ , a region exists in the high  $(K, d_0)$  parameter space where the lattice structure is dominant, characterized by large lattice constants (i.e., the average distance between neighboring unit cells) and large unit cell volumes (i.e., the area occupied by particles within a unit cell). Within this region, the lattice constant increases with  $d_0$  but remains largely insensitive to  $K$ . Conversely, the unit cell volume decreases as  $K$  increases but shows little dependence on  $d_0$ . Outside this region, the lattice structure becomes recessive, and the system tends to revert to a more uniform state. The boundary between these two regimes can be approximated by relation (20) (see Sec. 6 for details), which reflects a balance between the spatial periodicity of pattern formation and the spatial dynamics of the particles. The sawtooth shape of this boundary arises from the discrete nature of the wavenumber  $k_n = 2\pi n/L$  in a finite system with periodic boundary conditions.

Interestingly, even in the recessive region, where the system appears macroscopically uniform, it still exhibits microscopic hyperuniformity, as shown in Fig. 6(e), which is the final state of a random uniform initial conditions (see Fig. 6(d)). To quantify the degree of order in hyperuniformity, we computed the structure factor  $S(q) = N^{-1} \sum_{i,j=1}^N e^{i\mathbf{q} \cdot (\mathbf{r}_i - \mathbf{r}_j)}$  and density variance  $\langle \delta \rho^2(R) \rangle = \langle [\rho(R) - \langle \rho(R) \rangle]^2 \rangle$ ,

which are standard measures for characterizing hyperuniformity[10, 11]. As shown in Fig. 6(f) and (g), the recessive lattice states for large coupling strength and small coupling radius ( $K = 20, d_0 = 0.1, 0.25$ ) exhibit a scaling behavior of  $S(q \rightarrow 0) \sim q^2$ , and  $\langle \delta\rho^2(R \rightarrow \infty) \rangle \sim R^{-3}$ , which is characteristic of class I hyperuniformity [10]. While for smaller coupling strength ( $K = 1$ ), the system shows a scaling behavior of  $S(q \rightarrow 0) \sim q^0$ , and  $\langle \delta\rho^2(R \rightarrow \infty) \rangle \sim R^{-2}$ , indicating Poisson-like density fluctuations. This suggests that a stronger coupling strength is easier to induce hyperuniformity in the recessive lattice. It should be noted that the high  $K$  is not a necessary condition, as discussed in Sec. 6, where the instability condition for the random uniform state is independent of  $K$ .

## 5 Initial conditions determined cells composition [In future publications]

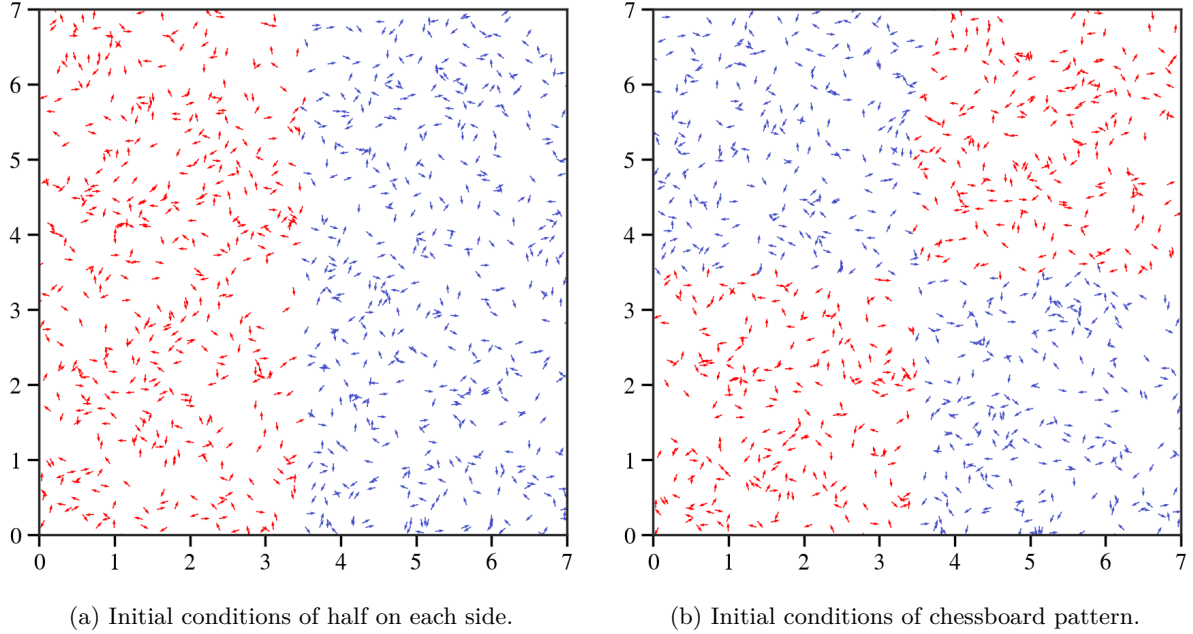


Figure 7: Two artificial non-uniform initial conditions in space. Red and blue particles represent particles with positive and negative chirality, respectively.

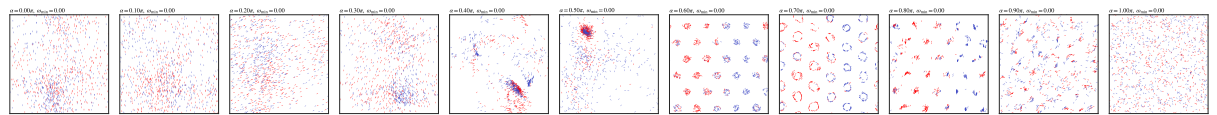


Figure 8: Snapshot of the system at  $t = 80$  with  $N = 1000$ ,  $K = 20$ ,  $\omega_{\min} = 0$ ,  $\Delta\omega = 1$  and initial conditions of half on each side.

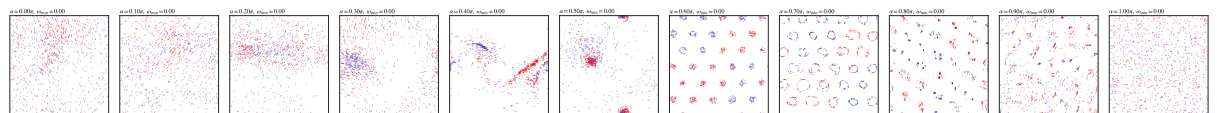


Figure 9: Snapshot of the system at  $t = 80$  with  $N = 1000$ ,  $K = 20$ ,  $\omega_{\min} = 0$ ,  $\Delta\omega = 1$  and initial conditions of chessboard pattern.

## 6 Critical transition and mechanism

In the thermodynamic limit  $N \rightarrow \infty$ , the state of the system in Eq. (1) can be characterized by the single-partial distribution  $\rho(\mathbf{r}, \theta, t)$ , which satisfies the continuity equation

$$\frac{\partial \rho}{\partial t} = -v \mathbf{p}(\theta) \cdot \nabla \rho - \frac{\partial}{\partial \theta} \{ \mathcal{T}[\rho] \rho \} , \quad (9)$$

where  $\mathcal{T}$  is the linear operator that has the form

$$\begin{aligned} \mathcal{T}[\rho] = & \frac{K}{A} \int_{L \times L} d^2 \mathbf{r}' \int_0^{2\pi} d\theta' \rho(\mathbf{r}', \theta', t) \\ & \times \Theta(d_0 - |\mathbf{r}' - \mathbf{r}|) [\sin(\theta' - \theta + \alpha) - \sin \alpha] , \end{aligned} \quad (10)$$

where  $\Theta(r)$  is Heaviside step function and

$$A = \int_{L \times L} d^2 \mathbf{r}' \int_0^{2\pi} d\theta' \rho(\mathbf{r}', \theta', t) \Theta(d_0 - |\mathbf{r}' - \mathbf{r}|) . \quad (11)$$

One obvious solution of Eq. (9) is  $\rho = (2\pi L^2)^{-1}$  representing a uniform disordered state. The stability of such a solution can be investigated by considering a small perturbation,

$$\rho(\mathbf{r}, \theta, t) = \frac{1}{2\pi L^2} + \varepsilon e^{\lambda(k)t+i\mathbf{k}\cdot\mathbf{r}} \Phi(\theta) , \quad (12)$$

with  $k = |\mathbf{k}| > 0$ , and linearizing the non-linear continuity equation (9), obtaining a eigenvalues problem to compute the  $\lambda(k)$  spectrum

$$(\mathcal{L}_0 - ivk\mathcal{L}_1) \Phi = \lambda \Phi , \quad (13)$$

$\mathcal{L}_0$  is diagonal in the basis  $\{e^{im\theta}\}_{m=-\infty}^\infty$ ,

$$\mathcal{L}_0 \Phi_m = \lambda_m^{[0]} e^{im\theta} , \quad (14)$$

with the eigenvalues

$$\lambda_m^{[0]}(k) = \frac{K J_1(kd_0)}{kd_0} (\delta_{m,-1} e^{i\alpha} + \delta_{m,1} e^{-i\alpha}) , \quad (15)$$

where  $J_1(x)$  is the Bessel function of the first kind of order one. The operator  $\mathcal{L}_1$  is defined as

$$\mathcal{L}_1 e^{im\theta} = \frac{1}{2} (e^{i(m+1)\theta-i\vartheta} + e^{i(m-1)\theta+i\vartheta}) , \quad (16)$$

where  $\vartheta$  is the forms  $\mathbf{k}$  with the  $x$  axis. Without the loss of generality, we can define the  $x$  axis parallel to  $\mathbf{k}$ , and, therefore, take  $\vartheta = 0$ .

Therefore, we have the characteristic polynomial

$$P_{2M+1}(\lambda) = \begin{vmatrix} \lambda_{-M}^{[0]} - \lambda & b & \dots & 0 \\ b & \lambda_{-M+1}^{[0]} - \lambda & b & \vdots \\ \vdots & b & \ddots & b \\ 0 & \dots & b & \lambda_M^{[0]} - \lambda \end{vmatrix} , \quad (17)$$

where  $b = -ikv/2$ . For analytical convenience, we truncate the expansion at order  $M = 2$ , resulting in a 5-th degree polynomial  $P_5(\lambda)$  with the following coefficients:

$$\begin{aligned} c_5 &= 1, \quad c_4 = -\frac{2KJ_1(d_0k)\cos\alpha}{d_0k}, \quad c_3 = \frac{K^2 J_1^2(d_0k)}{d_0^2 k^2} + k^2 v^2 \\ c_2 &= -\frac{Kkv^2 J_1(d_0k)\cos\alpha}{d_0}, \quad c_1 = \frac{3k^4 v^4}{16}, \quad c_0 = 0 . \end{aligned} \quad (18)$$

It is evident that  $\lambda = 0$  is always a root of the characteristic polynomial. To analyze the signs of the remaining eigenvalues, we factor out this zero root and apply the Routh–Hurwitz criterion to the reduced

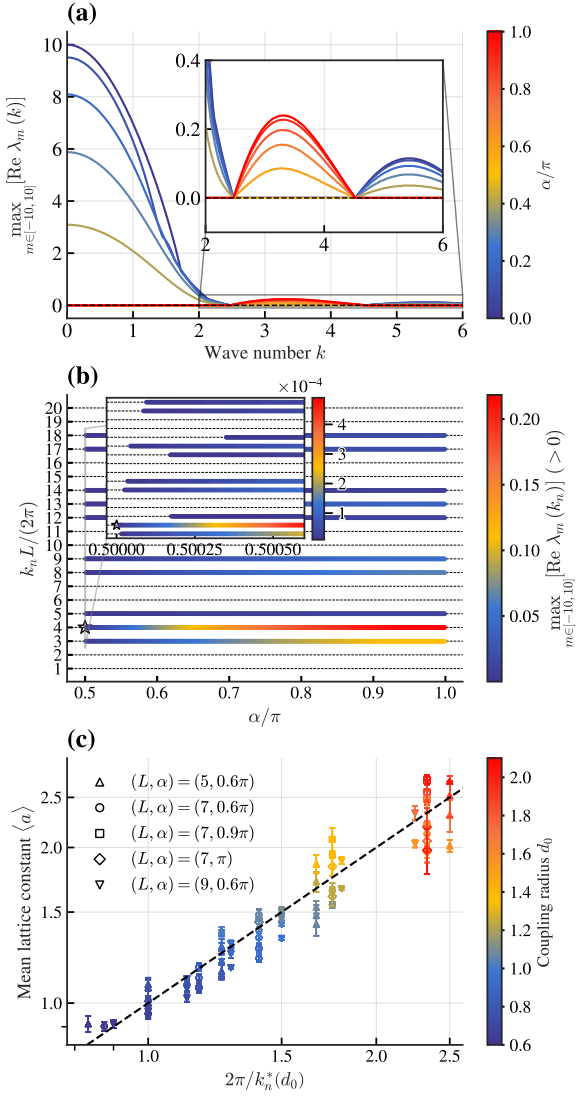


Figure 10: (a)-(b) Computations of the  $\lambda(k)$  with the largest real part as a function of the continuous wavenumber  $k$  [(a)] and standardized discrete wavenumber  $\bar{k}L/(2\pi)$  [(b)] and  $\alpha$  in the truncated basis  $M = 10$ . Other parameters as in Fig. 1. Insets: magnified views. (b) Thick colored lines denote positive eigenvalues (unstable modes), while thin dashed lines indicate stable modes. Stars mark the first unstable wavenumber at criticality. (c) Measured mean lattice constant  $\langle a \rangle$  compared to theoretical prediction. Horizontal and vertical error bars represent standard deviations across  $K$  and unit cells, respectively. The black dashed line indicates a 1:1 correspondence.

polynomial  $P_4(\lambda) = c_5\lambda^4 + \dots + c_2\lambda + c_1$ . This yields a necessary and sufficient condition for system stability:

$$J_1(d_0k) \cos \alpha < 0. \quad (19)$$

This inequality indicates that stability depends on the interplay between the frustration  $\alpha$  and coupling distance  $d_0$ , but is independent of both the coupling strength  $K$  and self-propulsion speed  $v$ .

As shown in Fig. 10(a), for  $\alpha < \pi/2$ , both the instability and the maximum growth rate occur at  $k = 0$ , corresponding to a type III instability [1], which does not lead to pattern formation in an essential way. In contrast, for  $\alpha > \pi/2$ , we examine the discriminant  $\Delta$  of the cubic polynomial  $P_3(\lambda) = P'_4(\lambda)$  and find that  $\Delta < 0$  for all  $k, K$  and  $d_0$ , indicating the presence of at most one real root of  $P_4(\lambda)$ . But Descartes' rule of signs shows that  $P_4(\lambda)$  has an even number of positive roots, which means that there is no positive real root, and the instability must arise from a pair of complex conjugate roots with positive real parts. This corresponds to a II<sub>*o*</sub> instability (also known as Hopf–Turing bifurcation), which gives rise to spatiotemporal patterns. In our system, this instability manifests dominantly as respiration motions of the lattice states. Overall, the frustration parameter  $\alpha$  serves as the key control parameter for the emergence of lattice structures, with a critical point at  $\alpha = \pi/2$ .

And as illustrated in Fig. 10(a) and (b), the most unstable wave number  $k^*/k_n^*(d_0)$  (periodic boundary conditions require discrete wavenumbers  $k_n = 2\pi n/L$  with  $n = 1, 2, \dots$ ) is insensitive to the value of  $\alpha (> \pi/2)$ . Therefore, it can be considered that the patterns occur on a long length scale near the threshold  $\alpha = \pi/2$ , and they are spatially periodic with similar properties, which is consistent with the numerical results shown in Fig. 10(c) that the lattice constant of different  $\alpha, K$  is nearly identical and can be predicted by the wavelength  $2\pi/k_n^*(d_0)$ .

Significantly, apart from spatial periodicity, the volume of the unit cell is another important characteristic of the lattice state. Near the critical point  $\alpha = \pi/2$ , the spatiotemporal distribution of phases is similar to that of the uniform state (see Fig. 1(d)), where the effective rotational radius of particles is approximately  $v/|\dot{\theta}_i| \approx v/K$ . Therefore, the critical condition for the emergence of dominant lattice states can be estimated by balancing the spatial periodicity of pattern formation and spatial dynamics of particles. The transition happens to be two unit cells tangent to each other:

$$\frac{2\pi}{k^*(d_0)} = \frac{2v}{K}, \quad (20)$$

which is consistent with the numerical results shown in Fig. 6(a)–(c). When the wavelength is too short to overcome the volume of the cells, the cells overlap together, resulting in macroscopic uniformity, but it still possesses unstable pattern-forming modes, resulting in microscopic hyperuniformity.

## 7 Conclusions

In summary, we have investigated a system of self-propelled particles with local phase interactions and phase frustration  $\alpha$ . Our study reveals that  $\alpha$  plays a crucial role in determining the collective behavior of the system, leading to the emergence of various spatiotemporal patterns, including globally synchronized states, swarming states, and lattice structures, which can be further classified into dominant and recessive lattice states based on the coupling strength  $K$  and coupling radius  $d_0$ . Notably, we identified a critical transition at  $\alpha = \pi/2$ , beyond which the system exhibits a Hopf–Turing bifurcation, resulting in the formation of hexagonal lattice patterns characterized by respiration or dual-lane self-propelled motions in space and uniform incoherent distribution or dual-cluster synchronization in phase. The emergence of these patterns is governed by different values of  $\alpha > \pi/2$ .

Furthermore, we discovered that even in regimes where the lattice structure is recessive, the system exhibits hyperuniformity, characterized by suppressed density fluctuations at large scales. This hyperuniformity arises from the interplay between phase frustration and local interactions, highlighting the intricate relationship between activity and order in active matter systems. Our findings contribute to a deeper understanding of the mechanisms underlying pattern formation and hyperuniformity in active matter, with potential implications for designing materials with novel properties.

## References

- [1] M. C. Cross and P. C. Hohenberg. Pattern formation outside of equilibrium. *Rev. Mod. Phys.*, 65:851–1112, Jul 1993.
- [2] Daniel Escaff. Anti-aligning interaction between active particles induces a finite wavelength instability: The dancing hexagons. *Phys. Rev. E*, 109:024602, Feb 2024.
- [3] Daniel Escaff. Self-organization of anti-aligning active particles: Waving pattern formation and chaos. *Phys. Rev. E*, 110:024603, Aug 2024.
- [4] Daniel Escaff and Rafael Delpiano. Flocking transition within the framework of kuramoto paradigm for synchronization: Clustering and the role of the range of interaction. *Chaos: An Interdisciplinary Journal of Nonlinear Science*, 30(8):083137, 08 2020.
- [5] Nikita Kruk, José A. Carrillo, and Heinz Koepll. Traveling bands, clouds, and vortices of chiral active matter. *Phys. Rev. E*, 102:022604, Aug 2020.
- [6] Nikita Kruk, Yuri Maistrenko, and Heinz Koepll. Self-propelled chimeras. *Phys. Rev. E*, 98:032219, Sep 2018.
- [7] D. Levis, I. Pagonabarraga, and B. Liebchen. Activity induced synchronization: Mutual flocking and chiral self-sorting. *Phys. Rev. Res.*, 1:023026, Sep 2019.
- [8] Benno Liebchen and Demian Levis. Collective behavior of chiral active matter: Pattern formation and enhanced flocking. *Phys. Rev. Lett.*, 119:058002, Aug 2017.
- [9] Hidetsugu Sakaguchi, Shigeru Shinomoto, and Yoshiki Kuramoto. Mutual entrainment in oscillator lattices with nonvariational type interaction. *Progress of Theoretical Physics*, 79(5):1069–1079, 05 1988.
- [10] Salvatore Torquato. Hyperuniform states of matter. *Physics Reports*, 745:1–95, 2018. Hyperuniform States of Matter.
- [11] Salvatore Torquato and Frank H. Stillinger. Local density fluctuations, hyperuniformity, and order metrics. *Phys. Rev. E*, 68:041113, Oct 2003.
- [12] Bruno Ventejou, Hugues Chaté, Raul Montagne, and Xia-qing Shi. Susceptibility of orientationally ordered active matter to chirality disorder. *Phys. Rev. Lett.*, 127:238001, Nov 2021.
- [13] Yujia Wang, Bruno Ventéjou, Hugues Chaté, and Xia-qing Shi. Condensation and synchronization in aligning chiral active matter. *Phys. Rev. Lett.*, 133:258302, Dec 2024.